

# Full-cycle device-scale simulations of memory materials with a tailored atomic-cluster-expansion potential

Yuxing Zhou,<sup>1</sup> Daniel F. Thomas du Toit,<sup>1</sup> Stephen R. Elliott,<sup>2</sup> Wei Zhang,<sup>3,\*</sup> and Volker L. Deringer<sup>1,\*</sup>

<sup>1</sup>*Inorganic Chemistry Laboratory, Department of Chemistry, University of Oxford, Oxford OX1 3QR, United Kingdom*

<sup>2</sup>*Physical and Theoretical Chemistry Laboratory, Department of Chemistry, University of Oxford, Oxford OX1 3QZ, United Kingdom*

<sup>3</sup>*Center for Alloy Innovation and Design (CAID), State Key Laboratory for Mechanical Behavior of Materials, Xi'an Jiaotong University, Xi'an 710049, China*

\*E-mail: wzhang0@mail.xjtu.edu.cn; volker.deringer@chem.ox.ac.uk

**Computer simulations have long been key to understanding and designing phase-change materials (PCMs) for memory technologies. Machine learning is now increasingly being used to accelerate the modelling of PCMs, and yet it remains challenging to simultaneously reach the length and time scales required to simulate the operation of real-world PCM devices. Here, we show how ultra-fast machine-learned interatomic potentials, based on the atomic cluster expansion (ACE) framework, enable simulations of PCMs reflecting applications in devices with excellent scalability on high-performance computing platforms. We report full-cycle simulations—including the time-consuming crystallisation process (from digital “zeroes” to “ones”)—thus representing the entire programming cycle for cross-point memory devices. We also showcase a simulation of full-cycle operations, relevant to neuromorphic computing, in a mushroom-type device geometry. Our work provides a springboard for the atomistic modelling of PCM-based memory and neuromorphic computing devices—and, more widely, it illustrates the power of highly efficient ACE ML models for materials science and engineering.**

Phase-change materials (PCMs) from the Ge–Sb–Te system have been widely used in emerging electronic devices, including non-volatile memory and neuromorphic in-memory computing technologies<sup>1–6</sup>. Driven by Joule heating resulting from the application of electric pulses, the SET (crystallisation) and RESET (amorphisation) operations are associated with fast and reversible transitions between the amorphous (low-conductance) and crystalline (high-conductance) states of PCMs. A large property contrast between these states encodes “zeroes” and “ones” in the atomic structure, respectively, for binary memory<sup>7</sup>. Furthermore, finely tuning the conductance of PCM cells between all-amorphous and all-crystalline states enables multi-level programming for neuromorphic in-memory computing<sup>8</sup>.

The switching processes in PCMs can be completed within nanoseconds—that is, within time scales accessible for molecular-dynamics (MD) computer simulations—and this has long made PCMs a prime application area in the field of materials modelling. Density-functional theory (DFT)-driven *ab initio* molecular-dynamics (AIMD) simulations have played a key role in understanding structural features<sup>9–11</sup>, property contrast<sup>12–15</sup>, and crystallisation kinetics<sup>16–18</sup> of PCMs based on representative small-scale models (typically containing on the order of 1,000 atoms or fewer)<sup>18</sup>. Building on the long-standing successes of DFT and AIMD, machine-learning (ML)-based interatomic potentials have recently emerged which accelerate first-principles atomistic modelling by many orders of magnitude<sup>19–21</sup>, and which can therefore provide new insights at much-extended time and length scales.

More than a decade ago already, Sosso *et al.* reported the first ML potential for modelling PCMs, at that time for the binary compound GeTe<sup>22</sup>, based on the Behler–Parrinello neural-network framework<sup>23</sup>. Since then, ML-driven MD simulations have become gradually more established: for example, they revealed details of the temperature-dependent crystallisation in GeTe<sup>24</sup> and Ge<sub>2</sub>Sb<sub>2</sub>Te<sub>5</sub> alloys<sup>25</sup>. In time, more ML potentials have begun to be developed for different PCMs<sup>25–29</sup>. We recently reported a chemically transferable and defect-tolerant ML

potential for Ge–Sb–Te (GST) materials along the GeTe–Sb<sub>2</sub>Te<sub>3</sub> tie-line, fitted using the Gaussian approximation potential (GAP) framework<sup>30</sup> and based on a comprehensive structural dataset and iterative training<sup>31</sup>. A neuro-evolution potential was recently developed for large-scale crystallisation simulations of Sb<sub>2</sub>Te, SbTe, and Sb<sub>2</sub>Te<sub>3</sub>, revealing distinct behaviours driven by nucleation and growth<sup>32</sup>. More generally, graph-based ML methods constitute the current state-of-the-art architectures in terms of accuracy and chemical transferability<sup>33,34</sup>, and they have begun to attract attention in the PCM community for general-purpose simulation tasks<sup>35</sup>.

In 2025, computational modelling is now often able to describe “the real thing” thanks to ML-driven potentials<sup>36</sup>, and yet these models still face a significant obstacle when it comes to describing PCMs in a fully realistic way—e.g., because of the length scales and structural complexity associated with applications in this domain. Complex simulation protocols are therefore required to model PCM devices, such as non-isothermal heating, which we have demonstrated for both cross-point- and mushroom-type cells<sup>31</sup>. Using the GST-GAP-22 potential at the time, we simulated a 50-picosecond RESET operation (“1→0”), showing non-isothermal melting and rapid cooling in a 532,980-atom model, representing a cell volume of  $20 \times 20 \times 40 \text{ nm}^3$  in cross-point memory devices<sup>31</sup>. However, the subsequent SET (“0→1”) typically requires tens of nanoseconds, rather than tens of picoseconds, to complete in devices. Performing a crystallisation run over 10 ns for the same structural model, with GST-GAP-22, would have consumed more than 150 million CPU core hours by our estimate. This type of excessive cost (in terms of time, financial cost, and carbon emissions) would clearly make the use of GST-GAP-22 unfeasible for full-cycle modelling of GST devices.

Herein, we show how one can simultaneously reach both the length and time scales in simulations of switching operations in real-world GST devices, leveraging the atomic-cluster-expansion (ACE) ML framework<sup>37</sup>. The substantial speed-up by moving from the GAP to the ACE framework<sup>38</sup> enables atomistic simulations reflecting device applications on widely

available CPU-based computing systems. We have thus outlined an “off-the-shelf”-usable ML approach for the community to study the switching mechanisms of GST-based devices. Beyond PCMs, our work explores the current frontiers of ultra-large-scale all-atom simulations for materials science and engineering.

## Results

### Fast and CPU-efficient simulations with an optimised ACE potential

We used the ACE framework to develop a computationally efficient ML model for GST. In ACE, the local environment of a given atom is encoded using a many-body expansion (Fig. 1a). The atomic environment is expressed in terms of radial functions and spherical harmonics, translated into a linear combination of so-called “A-basis” functions, and subsequently into invariant “B-basis” functions by coupling via the generalized Clebsch–Gordan coefficients. A linear combination of B-basis functions is called the “property” of a given atomic environment in the context of ACE. The energy of the atom is predicted as a function of atomic properties, using a linear (depending on just one single property) or nonlinear embedding. The complexity of ACE models is therefore controlled by the numbers of basis and embedding functions; more details of the framework can be found in Refs. <sup>37,39–41</sup>.

Inference in ACE essentially requires summation operations (Fig. 1a) and avoids computationally expensive tasks (e.g., Gaussian process regression in GAP<sup>42</sup>). Hence, ACE models are computationally highly efficient: they can be more than  $100 \times$  faster than GAP on CPU cores while achieving the same level of numerical accuracy<sup>39,43</sup>. We recently developed an initial ML potential for elemental tellurium using GAP, and then re-fitted the reference data using ACE, to study crystallisation and melting in Te-based selector devices<sup>44</sup>. Here, we address the structurally and chemically more complex GST system, starting from the existing GST-GAP-22 dataset—which incorporates relevant domain knowledge<sup>31</sup>—and also making use of the ACE framework. However, simply re-fitting an ACE potential using the GST-GAP-22 training

data “out of the box” produced unphysical structural motifs in our tests (e.g., atomic clustering and phase segregation), and lost atoms in MD simulations. We believe that this is due to two reasons: first, the hyperparameters used in ACE are complex and can be difficult to tune manually (cf. Supplementary Table 2); second, an ACE model may require more training structures than GAP<sup>45</sup>. The usefulness of ACE potentials in the field of GST materials has been demonstrated recently<sup>38</sup>: the authors focused on the use of a previously proposed indirect-learning approach for ML potentials<sup>46</sup> and built upon the GST-GAP-22 dataset and model<sup>31</sup>, reporting efficient ACE potentials which were applied to the  $\text{Ge}_2\text{Sb}_2\text{Te}_5$  compound<sup>38</sup>.

In the present work, we focus on an alternative route, both optimising the hyperparameters of the model and extending the DFT training dataset (Fig. 1b). The GST-GAP-22 dataset was first re-labelled using DFT with the Perdew–Burke–Ernzerhof (PBE) exchange–correlation functional<sup>47</sup> that is widely used in simulations of PCMs. We then added further AIMD configurations of disordered GST (taken from Ref. <sup>31</sup>) and fitted initial ACE models to the combined data, using the XPOT software to optimise hyperparameters (Methods)<sup>48,49</sup>. Starting from this well-parameterised ACE model (denoted “iter-0”), we carried out three domain-specific iterations (iter-1 to iter-3) to include melt-quenched disordered structures and intermediate configurations during phase-transition processes (Fig. 1b). We also added small-scale hard-sphere random structures (6–40 atoms) with small atomic distances, generated using the `buildcell` code of *ab initio* random structure searching (AIRSS)<sup>50,51</sup>, for iter-1 to iter-3, to make the ACE models more robust<sup>43</sup>. In addition, we carried out ACE-driven random structure search (ACE-RSS), akin to previously described GAP-driven RSS<sup>52–54</sup>, in two further iterations (iter-4 and iter-5). We refer to our final ACE potential model as “GST-ACE-24”. With its training dataset covering multiple GST compositions, we found that our GST-ACE-24 model is chemically transferable along the entire  $\text{GeTe}$ – $\text{Sb}_2\text{Te}_3$  tie-line: it can accurately capture different structural

properties of various amorphous GST compounds, as validated against AIMD (Methods and Supplementary Fig. 4).

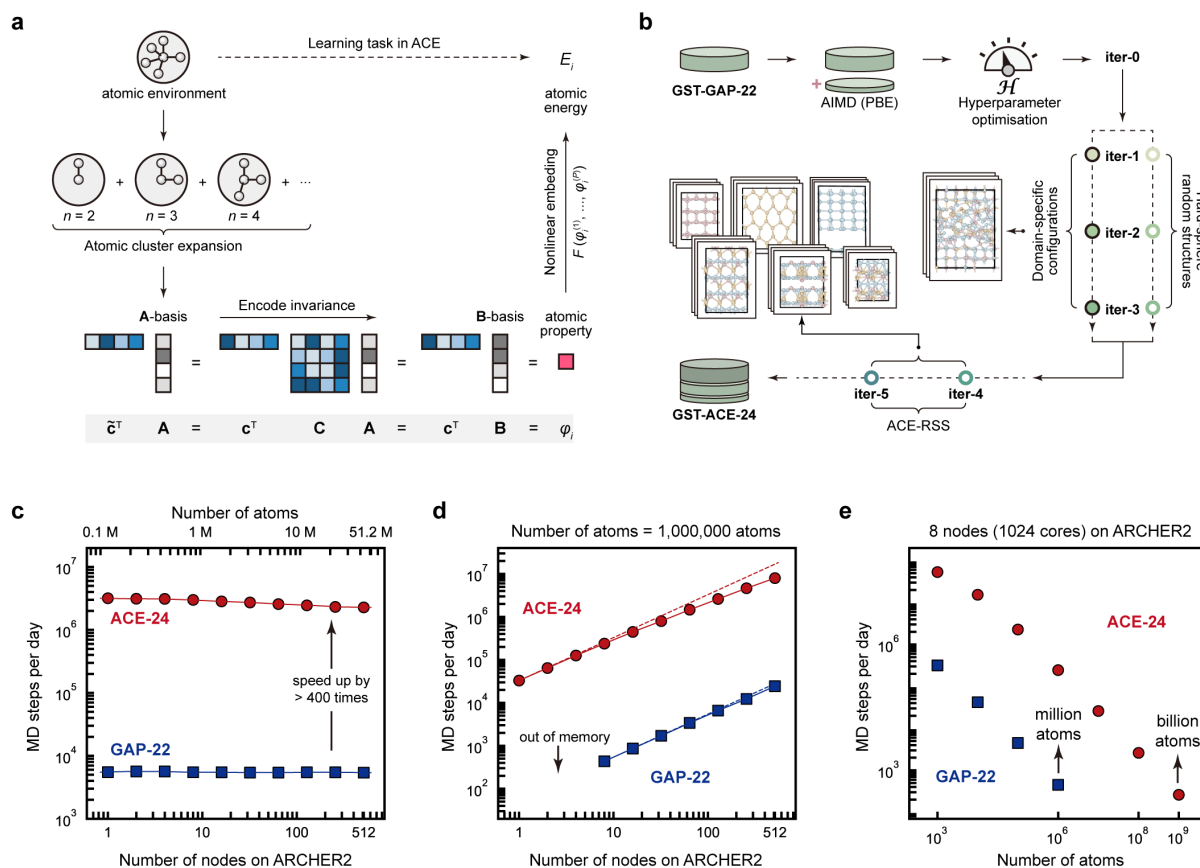


**Fig. 1 | An optimised atomic-cluster-expansion (ACE) ML potential for Ge–Sb–Te phase-change materials.** (a) Schematic overview of the learning task in ACE ML potential models. (b) The fitting protocol used for a new ACE potential of GST. Multistep iterations were carried out to expand the reference dataset. Insets show typical configurations for domain-specific iterations and ACE-RSS structures. Ge, Sb, and Te atoms are rendered as light red, light yellow, and light blue, respectively. Details are given in Supplementary Note 1. Different tests of computational efficiency on the ARCHER2 high-performance computing system were carried out for the GST-ACE-24 and GST-GAP-22 potentials, including: (c) weak scaling (at 100,000 atoms per node); (d) strong scaling up to 512 nodes—the maximum accessible for a single job on ARCHER2—for a 1-million-atom structural model; and (e) MD steps per day as a function of system size running on 8 computing nodes (1,024 CPU cores). The GAP-MD tests in panel (d) failed on configurations with 4 or fewer nodes due to insufficient memory.

To evaluate the computational efficiency of GST-ACE-24, we performed weak and strong scaling tests on ARCHER2, a high-performance computing system in the UK (Methods and

Supplementary Note 2). We found that, compared to GST-GAP-22, GST-ACE-24 offers more than  $400 \times$  higher efficiency on this large-scale CPU architecture (Fig. 1c). Both ACE and GAP showed reasonable scaling behaviour up to 512 nodes (65,536 CPU cores) in strong scaling tests for a structural model of 1 million atoms (Fig. 1d). An efficiency drop-off from the ideal scaling behaviour occurred for the ACE model when handling “small” structures (e.g., 100,000 atoms) on many computing nodes (Supplementary Fig. 1), because ACE is so fast that the inter-processor communication outweighs the computational cost of predicting energies and forces. For example,  $\approx 30\%$  of CPU time was used in inter-processor communication when simulating a 100,000-atom structural model on more than 128 nodes. In addition, we found the system-size limit for a total memory of 512 GB to be  $\approx 450,000$  atoms with GAP, whereas for the same hardware the limit was  $\approx 650$  million atoms with ACE. Hence, ACE is memory-efficient and enables billion-atom MD simulations (Fig. 1e) with only modest computational resources (e.g., 8 nodes on ARCHER2).

Moreover, ACE can also be used on GPU hardware, and its speed compares favourably to state-of-the-art graph-neural-network architectures: our ACE model is about  $6 \times$  faster than an equivariant neural-network potential we directly re-fitted for comparison, using the same training data as for GST-ACE-24 and the MACE architecture<sup>34,55</sup>, when testing on an NVIDIA A100 GPU card (Methods). We found the system-size limit for a total memory of 80 GB to be  $\approx 92$  million atoms with ACE on GPU, smaller than the limit on CPU ( $\approx 650$  million atoms). Hence, while ACE-MD can be run on GPU, its excellent scaling behaviour across multiple CPU nodes and the potential large memory capacity of CPU nodes make it particularly suitable for device-scale MD simulations on existing CPU hardware.

For practical MD simulations, we emphasise the importance of the robustness of ACE models: ACE-MD simulations will fail when atoms are lost due to inaccurately predicted energies and forces. This usually stems from insufficient training data for complex atomic

environments with small atomic distances. We designed a protocol to quantify the robustness of ACE models via high-temperature annealing: starting with a hard-sphere random structure of 1,000 atoms, the model was annealed at 3,000 K for 500 ps. (We note that high- $T$  annealing is part of the melt–quench process to generate amorphous GST, allowing the simulation to visit high-energy configurations; we also note that high- $T$  MD has been used previously for stability tests<sup>56</sup>.) We tested the robustness of ACE models on 7 different GST compositions, from GeTe to Sb<sub>2</sub>Te<sub>3</sub>, and performed 10 independent high- $T$  annealing runs for each composition. Despite gradually adding hard-sphere random structures to the training dataset, no successful runs were observed from iter-1 to iter-3: very close interatomic contacts were found in the MD simulations (Fig. 2a), which led to extremely large forces and then lost atoms. However, the inclusion of ACE-RSS structures in the training is concomitant with some successful runs in iter-4 and consistently successful runs in iter-5, producing reasonable high- $T$  liquid GST structures (Fig. 2a).

### **Ablation studies for the ACE model**

In ML research, “ablation” studies mean gradually removing aspects of a complex model and testing the effect of that on the performance. Here, we report systematic ablation studies for ACE models, with an aim to more systematically understand the roles of newly added configurations and optimised hyperparameters in ACE models. We first carried out an ablation study for the removal of random structures (including the hard-sphere random and ACE-RSS structures) based on high-temperature annealing tests (Fig. 2b). We observed consistently successful runs when more than half of the random structures were retained. However, removing 75% of them resulted in a marked decrease in stability, and a model where no random structures were present showed almost no successful runs.

We note that removing random structures slightly improved the numerical accuracy in describing domain-relevant structures (e.g., in melt–quench and phase-transition processes), in terms of energies (up to 3 meV atom<sup>-1</sup>) and forces (up to 13 meV Å<sup>-1</sup>) in our ablation tests (Fig.



2c); however, for practical purposes, we do not expect that this small advantage will typically outweigh the risk of losing atoms described above. Hence, in the context of ongoing research on how datasets for ML potentials are best developed<sup>21,57–60</sup>, we highlight the key role of such small-scale RSS structures: not only as a starting point for fitting potentials<sup>53,60–63</sup>, but also as an effective *post-hoc* correction approach that can add substantial MD stability.

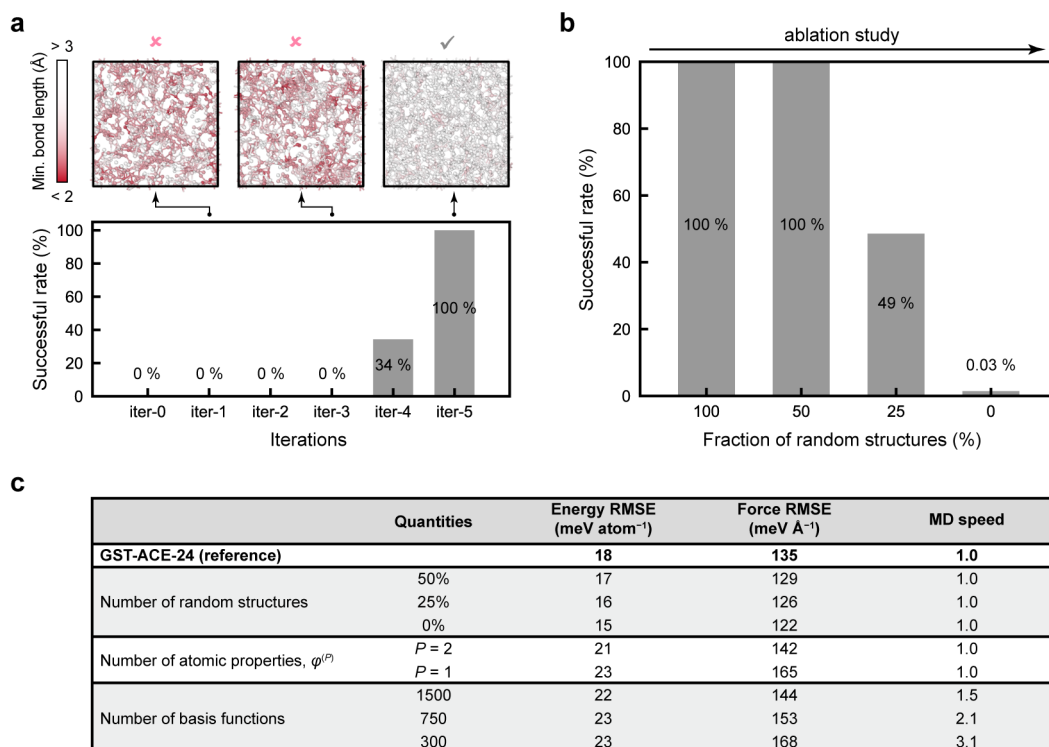


**Fig. 2 | Ablation studies for GST-ACE-24.** (a) Fraction of successful runs in high-temperature annealing tests for each iteration of the potential. Three structural models from different tests are shown, with atoms colour-coded by minimum bond length: red colour indicates atoms with very short distances to their nearest neighbour, which might lead to lost atoms in MD. (b) An ablation study for the number of random structures present in the training data, evaluated based on the fraction of successful high- $T$  annealing runs. (c) Ablation studies exploring varying numbers of: (i) random structures in the training; (ii) atomic properties (see also Ref. 45); and (iii) basis functions. We note that GST-ACE-24 serves as the reference model in the ablation study, which has 906 random structures (319 hard-sphere random and 587 ACE-RSS structures; Supplementary Table 1) in the training dataset,  $P = 3$  atomic properties, and 3,000 basis functions. Root-mean-square error (RMSE) values for energy and force predictions were calculated on the testing dataset that contains relevant configurations from melt-quench and phase-transition processes. The MD speed is given relative to that of GST-ACE-24.

We also carried out ablation studies for the complexity of ACE models. We changed the number of atomic properties,  $P$ , which controls how the atomic energy is constructed from the local atomic properties in a linear ( $P = 1$ ) or non-linear way ( $P \geq 2$ ). We fitted a linear ACE model and a simpler non-linear one with  $P = 2$ , and compared both resulting models against GST-ACE-24 ( $P = 3$ ). For the linear model, we found a force RMSE approximately 30 meV  $\text{\AA}^{-1}$  higher than for GST-ACE-24. We also compared ACE models with gradually reduced basis functions (to 1,500, 750, and 300, respectively). Although decreasing the number of basis functions increases the computational efficiency (Fig. 2c), fewer functions lead to larger numerical errors. Hence, we argue that our GST-ACE-24 model offers a favourable combination of robustness and accuracy for practical MD simulations.

### **Full-cycle operations for cross-point GST memory devices**

With the help of ACE, we are now able to simulate full-cycle operations in cross-point GST devices (Fig. 3a). We first reproduced a non-isothermal melt-quench (RESET) simulation that had previously been demonstrated for cross-point memory, using the GST-GAP-22 potential at the time<sup>31</sup>. As in Ref. <sup>31</sup>, we used a structural model of  $\text{Ge}_1\text{Sb}_2\text{Te}_4$  of  $20 \times 20 \times 40 \text{ nm}^3$  (532,980 atoms), which includes a fixed (here, amorphous) slab to prevent unwanted atomic migration across the periodic cell boundary (Supplementary Note 3)—resembling a thermal barrier in contact with GST in a real device (Fig. 3a).

We used the NVE ensemble (i.e., constant number of particles, volume, and energy) to simulate the RESET process. As shown in Fig. 3b, a 10-ps heating pulse (0.064 pJ) imposed on the model was first simulated by spatially inhomogeneously increasing the kinetic energy of atoms linearly along the  $z$ -axis, corresponding to a large temperature gradient from the bottom ( $> 1,000 \text{ K}$ ) to the top ( $\approx 300 \text{ K}$ ) of the 40-nm-long cell. To model the cooling process after removing the heating pulse, the added energy was then gradually removed from each atom over another 40 ps until reaching room temperature. The atoms in Fig. 3 are colour-coded, based on

the SOAP kernel similarity<sup>64</sup>, which was previously used to quantify per-atom crystallinity for GST<sup>18</sup>. Based on the ACE-MD trajectories, we found that almost all of the structural model turned into amorphous Ge<sub>1</sub>Sb<sub>2</sub>Te<sub>4</sub> after heating and cooling (Supplementary Fig. 2). Technical details of these non-isothermal heating and cooling simulations using NVE are given in Supplementary Note 3 and in our previous work<sup>31</sup>. We note that this RESET simulation using GST-ACE-24 and its evolution of temperature gradients is consistent with previous results using GST-GAP-22 (Supplementary Fig. 2)<sup>31</sup>, providing further validation of the approach.

We next simulated the SET process of the cross-point structural model. Unlike the short, intense RESET pulse (10 ps, 0.064 pJ) that generates a pronounced temperature gradient across the cell, the SET heating pulse has a much longer duration (e.g., tens of nanoseconds) and smaller amplitude, resulting in a lower temperature gradient and smaller fluctuations. Here, we simulated the crystallisation of the device-scale model using the NVT ensemble (i.e., constant number of particles, volume, and temperature). The crystallisation of undoped GST is known to be driven by homogeneous nucleation<sup>65</sup>, in which critical nuclei quickly form during a stochastic incubation process<sup>16</sup>. The latter is the bottleneck for crystallisation, which can be bypassed either by applying a low-voltage seeding pre-pulse<sup>66,67</sup> or by doping with a suitable transition-metal element<sup>68-72</sup>. We note that in previous nucleation simulations of GST using AIMD, enhanced sampling methods, e.g., meta-dynamics<sup>73,74</sup> or pre-embedded crystalline seeds<sup>69,75</sup>, were employed to accelerate, or circumvent, the formation of critical nuclei in small-scale structural models. GST-ACE-24 is able to describe nucleation in GST without such additional constraints. We annealed the device-scale structural model of amorphous GST at 600 K for 20 ns. At 600 K, tens of nucleation centres, with random grain orientations, spontaneously formed after a few nanoseconds. The crystal grains quickly grew at 3 ns, with grain sizes increasing further until 20 ns (Fig. 3c). The resulting SET state is a polycrystalline sample of rock-salt-

like GST. We counted 277 crystalline grains of different crystal orientations, and the average diameter was  $\approx 4.6$  nm.

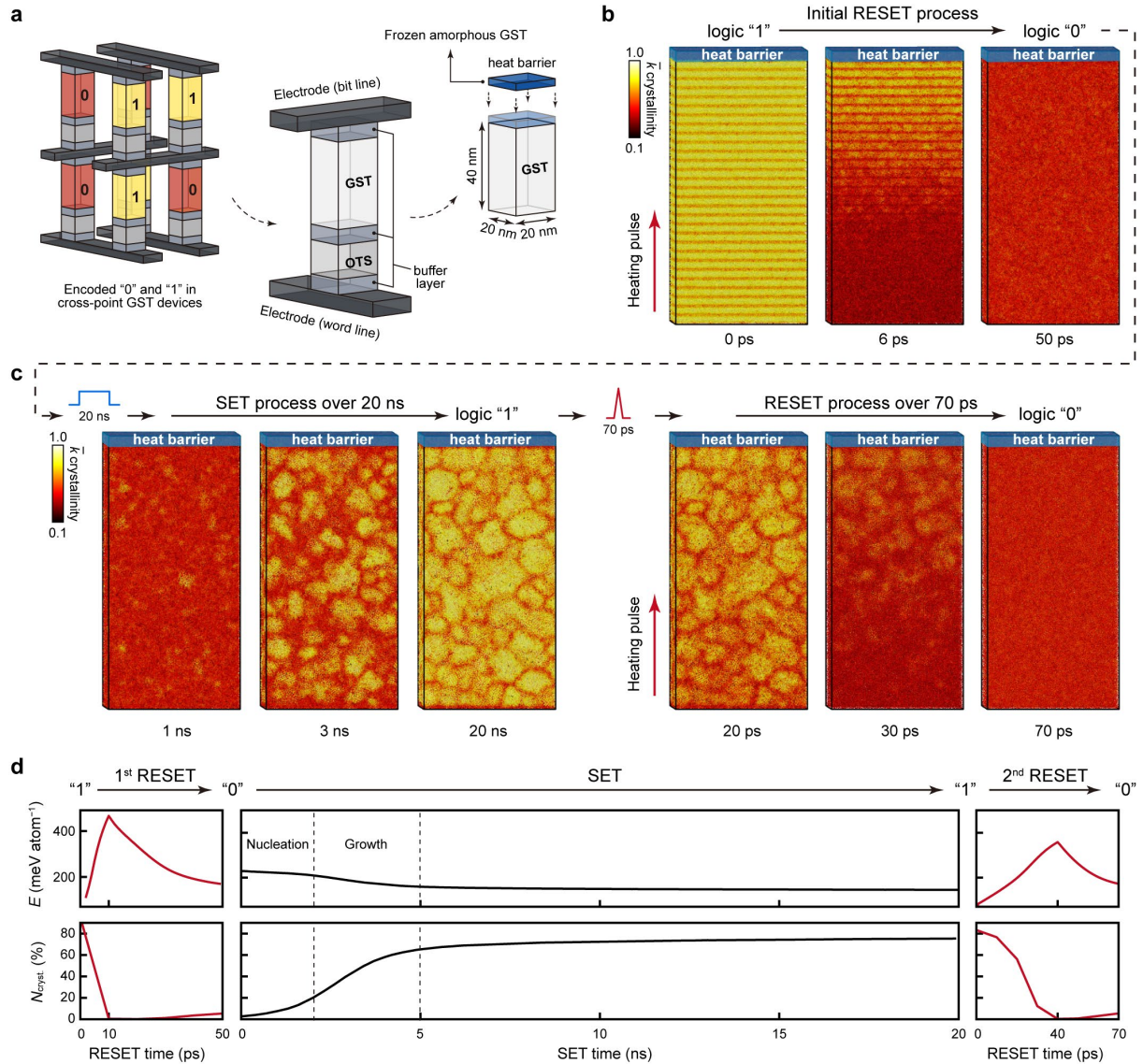


**Fig. 3 | Full-cycle device-scale simulations.** (a) Schematic of cross-point devices, in which logic “0” and “1” bits are encoded by amorphous and crystalline states of GST. In these devices, PCM layers and ovonic threshold switching (OTS) selector layers are sandwiched by buffer layers. A device-size structural model was built as in Ref. <sup>31</sup> ( $20 \times 20 \times 40$  nm $^3$ ; 532,980 atoms); note that we here use amorphous GST as a heat barrier. (b) The initial RESET operation, simulated similar to Ref. <sup>31</sup> but now using the GST-ACE-24 model, starting from layered trigonal Ge $_1$ Sb $_2$ Te $_4$ , triggered by a 10-ps heating pulse (0.064 pJ) from the bottom to the top. After the programming pulse, a 30-ps cooling was performed by removing the added kinetic energy from the structural model until it reached 300 K. (c) The subsequent SET operation at 600 K, simulated over 20 ns in the NVT ensemble. The resultant recrystallised GST structure contains 277 crystalline grains with an average diameter of  $\approx 4.6$  nm. A second RESET operation was then

simulated, via a 40-ps heating pulse (0.036 pJ) and a 30-ps cooling process (Supplementary Note 3). Colour coding in panels (b–c) indicates the SOAP-based<sup>64</sup> crystallinity measure,  $\bar{k}$  (see Ref. 18). (d) Computed potential energy and fraction of crystal-like atoms during the full-cycle simulations. A  $\bar{k}$  cut-off of 0.57 was used to separate crystal-like and amorphous-like atoms<sup>18</sup>. Dashed lines indicate the nucleation and growth processes during crystallisation.

We next simulated a second RESET process of the device-size model. We imposed a 40-ps heating pulse (0.036 pJ) to melt the recrystallised structure. The evolution of temperature profiles is shown in Supplementary Fig. 3. We note that the energy of this heating pulse (0.036 pJ) is smaller than that (0.064 pJ) initially used to erase the initial state of the cell (trigonal layered GST; cf. Fig. 3b); however, this smaller heating pulse still melted the whole structural model. The overall power consumption of both the first and the second RESET pulse is much lower than that in real devices, because the input power here is directly assigned to specific atoms to increase their kinetic energy. To program a device experimentally, the thermal energy is generated by Joule heating via electrical pulsing, which involves thermal dissipation and energy loss. Therefore, our ML-driven MD simulations provide the theoretical minimum energy values for RESET operations<sup>31</sup>. Nevertheless, the reduced RESET energy in our simulations implies that a polycrystal, with numerous rock-salt-like crystal grains, is much more easily melted than the stable trigonal phase of GST. We found that the structural disordering primarily occurred at the disordered grain boundaries, similar to the onset of the melting in simulations of re-crystallised, polycrystalline Te<sup>44</sup>. However, our ACE-MD simulations showed that the melting of GST also occurred inside the crystal grains; the latter has been suggested to stem from atomic migration and vacancy diffusion in rock-salt-like crystalline GST<sup>76</sup>.

We show the evolution of the potential energy and the fraction of crystal-like atoms during the ACE-MD simulated full-cycle operations in Fig. 3d. These properties provide a quantitative measure of the energetics involved in switching, and reveal the degree of structural ordering at different stages of the device operations. We estimate that the full-cycle simulations (i.e.,

RESET to SET and back to RESET) using ACE consumed  $\approx 770,000$  CPU core hours and  $\approx 2,500$  kWh running on ARCHER2 (cf. Ref. <sup>77</sup>). With more CPU resources available, it is feasible to simulate multiple SET–RESET cycles of GST-based binary memory devices, allowing atomic-scale investigations of structural and compositional variations over repeated full-cycle operations.

### **Full-cycle operations for in-memory computing**

Beyond their application in data-storage devices, GST alloys have also been used in neuromorphic in-memory computing tasks, which aim to process and store data directly within the same memory cell, thereby avoiding frequent data transfer between conventional memory and processing units<sup>4,5</sup>. In addition to binary ones and zeroes, in-memory computing requires multiple distinct intermediate logic states to represent (near-) continuous weights or values, which are essential for analogue computations (e.g., matrix–vector multiplications). In fact, the electrical-resistance level of GST depends on the ratio of the crystalline to the amorphous volume, making it possible to obtain multiple logic states via appropriate iterative RESET and cumulative SET operations. Such operations can be achieved using small-size bottom electrodes and large programming volumes in mushroom-type devices<sup>8</sup>. As shown in Fig. 4a, given a large programming volume, heating pulses of different amplitudes can thus create mushroom-like active regions with very different crystalline-to-amorphous ratios. Given that the diameter of the bottom electrode can be scaled down to  $\approx 3$  nm (Ref. <sup>78</sup>), the dimensions of state-of-the-art mushroom-type devices<sup>4,5</sup> could be further miniaturised, from hundreds to tens of nanometres—providing a broad, tuneable range of cell dimensions for optimisation.

Here, we demonstrate ACE-driven full-cycle simulations of such partial programming in mushroom-type cells. We simulated a cross-section of  $100 \times 40$  nm<sup>2</sup>, which represents the programming in the middle of a mushroom-type cell (Fig. 4b). We set the thickness of the slab model to 5 nm, corresponding to a quasi-two-dimensional periodic box. In total, this structural

model contains 794,808 atoms, much larger than the model size used to describe a mushroom-type geometry in our previous work<sup>31</sup>. The initial configuration is a rock-salt-like crystalline phase of  $\text{Ge}_1\text{Sb}_2\text{Te}_4$ , corresponding to an idealised single crystal with cation / vacancy disorder but no grain boundaries. A heat barrier ( $\approx 6$ -nm-thick slab of amorphous  $\text{Ge}_1\text{Sb}_2\text{Te}_4$ ) was added on the top of the cell, preventing atomic migration across the periodic boundary (Fig. 4b). To simulate programming operations, heating pulses with different magnitudes were added to regions of different sizes, representing separate logic states (Fig. 4c). We first added a small heating pulse (0.011 pJ) over 100 ps, resulting in a melted programming region with a diameter of  $\approx 50$  nm. This structural model was then quenched to 300 K over 200 ps by gradually removing kinetic energy from the structural model. We call the resulting intermediate state “logic state **I**”. We note that atoms outside the programming domain remained crystal-like after the heating process, leading to a large crystalline–amorphous interface (Fig. 4c).

We then simulated the crystallisation process for the logic state **I** at 600 K (Fig. 4d). Fast crystal growth proceeded at the crystalline–amorphous interface, leading to an evident shrinkage of the disordered-like region. Meanwhile, multiple nuclei were found inside the programming region. The crystalline seeds quickly grew in size, forming a polycrystalline domain. By distinguishing between atoms recrystallised through growth and those through nucleation, we observed a competition between growth-driven and nucleation-driven crystallisation (qualitatively similar to a recent preprint<sup>79</sup> based on a neural-network potential; see Discussion section for details). In our simulation, the growth-driven crystallisation accounts for 54% of the recrystallised atoms, whereas nucleation contributed 46% (Fig. 4e).

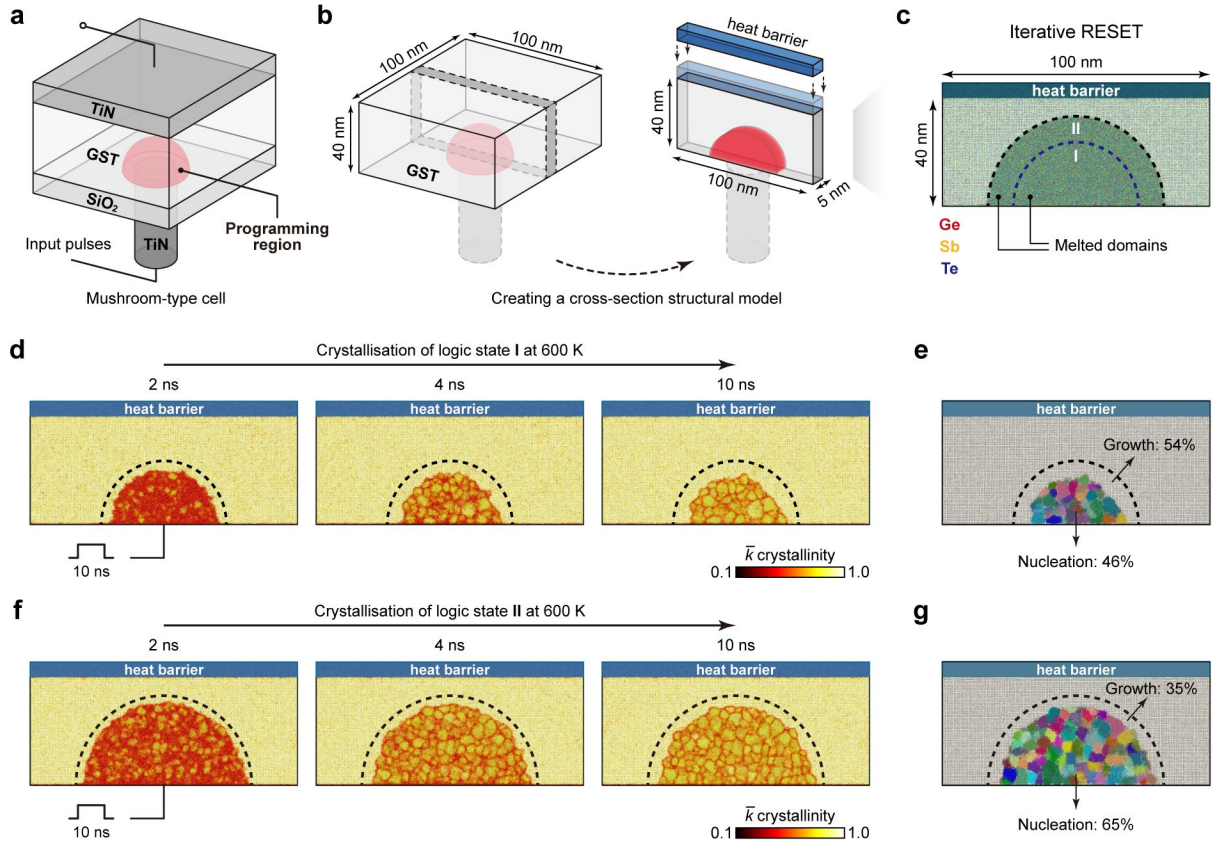


**Fig. 4 | Multiple logic states in a GST-based mushroom-type device.** (a) Schematic of mushroom-type cells, in which PCM layers are sandwiched by top and bottom electrodes (e.g., TiN). (b) A two-dimensional slice model<sup>31</sup> was built (here,  $100 \times 40 \times 5 \text{ nm}^3$ ; 794,808 atoms), which represents a cross-section of a mushroom-type cell. (c) Two different intermediate RESET states (viz. logic states **I** and **II**) were obtained after different 100-ps heating pulses (0.011 and 0.022 pJ, respectively) and the subsequent 200-ps cooling process. The two melted domains have diameters of  $\approx 50$  and  $\approx 70$  nm, respectively. Species-specific colour coding is used. (d) Crystallisation of the intermediate state **I** at 600 K over 10 ns. (e) Grain-segmentation analysis of the recrystallised intermediate state **I**. (f–g) As panels (d–e), but now for the intermediate state **II**. Colour-coding in panels (d, f) indicates the SOAP-based  $\bar{k}$  crystallinity, illustrating the amorphous-like (*red*) and crystalline-like domains (*yellow*). The grain analyses shown in panel (e, g) were carried out using polyhedral template matching<sup>80</sup> and grain-segmentation analyses, as implemented in OVITO<sup>81</sup>. Different colours indicate crystal grains with different orientations.

We next added a larger heating pulse (0.022 pJ) to the recrystallised model and cooled it down to 300 K, which created a larger melt-quenched glassy region with a diameter of  $\approx 70$  nm. We call this intermediate state “logic state **II**” (Fig. 4c). In its subsequent crystallisation at 600 K (Fig. 4f), the contributions from the growth and nucleation were 35% and 65%, respectively



(Fig. 4g). The increased nucleation contribution stems from the dominant nucleation-driven nature of the crystallisation in GST under these conditions. The larger the amorphous region, the more widespread the occurrence of homogeneous nucleation. This finding also implies that the SET speed in GST-based mushroom-type devices at 600 K is almost independent of the size of amorphised regions and the amplitude of the preceding RESET pulse. Rapid homogeneous nucleation is the key to such fast SET operations.

In fact, GST-based in-memory computing devices exhibit considerable resistance noise and time-dependent drift that erodes the precision and consistency of these devices<sup>82,83</sup>. On the one hand, the varied recrystallised morphologies, which contained crystal grains of different orientations (Fig. 4e and 4g), can be the source of stochasticity in cumulative SET operations, leading to cycle-to-cycle and device-to-device variations. On the other hand, the prominent resistance drift, believed to stem from structural relaxation of amorphous GST (known as ageing), can result in the overlap of two adjacent logic states, causing decoding errors<sup>84</sup>. We show in Supplementary Fig. 4 that our ACE model can well describe the degree of local bond-length asymmetry, sometimes referred to as Peierls distortions, of amorphous GST—a quantitative structural fingerprint of the ageing process<sup>85</sup>. Hence, our ACE model can simulate both stochastic recrystallisation and aged amorphous structures of mushroom-type devices, which provides atomic-scale insights into the programming mechanisms of GST-based mushroom-type devices for in-memory computing tasks.

## Discussion

Our ultrafast and chemically transferable ACE potential for GST alloys can serve as a powerful “off-the-shelf” simulation tool with quantum-mechanical accuracy. Its computational efficiency enables full-cycle simulations (multiple RESET to SET operations) of different device architectures at extensive length scales (tens of nanometres) and time scales (tens of nanoseconds). We expect that our ACE model can provide atomic-scale insights into realistic

programming conditions of GST-based devices, including repeated switching for binary memory applications, as well as cumulative SET and iterative RESET processes for neuromorphic in-memory computing. In the latter case, larger device geometries than in our current proof-of-concept simulation (Fig. 4) could make it possible to more finely tailor the amorphous-to-crystalline volume ratio to accommodate more resistance states. Simulating complex in-memory operations at the atomic scale could provide a more in-depth understanding of phase-change neuromorphic computing, and such simulations would benefit from fast and efficient ACE models.

We note that the atomistic modelling of PCMs on large length scales is gaining increasing interest in the community. From a technical perspective, the indirectly-learned ML potential of Ref. <sup>38</sup> already illustrated the usefulness of ACE in this domain: the authors reported the simulation of a  $\approx 1$ -million-atom bulk  $\text{Ge}_2\text{Sb}_2\text{Te}_5$  structure over 1 ns on combined CPU and GPU architectures, as well as the repeated switching of a  $\approx 100,000$ -atom bulk structure<sup>38</sup>. The scaling tests described in Ref. <sup>38</sup> are qualitatively consistent with our tests on the ARCHER2 high-performance computing system (Fig. 1c–e) where applicable, although (as the authors also note) the details will depend on the specific hardware. In terms of simulation cells and protocols reflecting PCM device geometries, a recent preprint described the use of a neural-network ML potential for  $\text{Ge}_2\text{Sb}_2\text{Te}_5$  (from Ref. <sup>25</sup>) and multiple GPU cards to perform large-scale simulations ( $\approx 2.8$  million atoms) over several nanoseconds<sup>79</sup>. A structural model was created by embedding an amorphous dome in a crystalline matrix to represent a mushroom-type device, and multiple thermostats were used to simulate SET operations<sup>79</sup>; a competition between nucleation and growth from the interface was identified<sup>79</sup>, which is qualitatively similar to Fig. 4. In our present work, we have combined a carefully optimised ACE potential that makes efficient use of CPU resources with advanced simulation protocols for cell geometries and programming conditions that are relevant to both cross-point and mushroom-type GST devices.

Looking back on the discussion of PCM modelling at the beginning of this paper, we note that ML-driven simulation methods have now been established in the field, allowing for wide-ranging simulation studies of functional materials, and increasingly becoming of relevance to experimental work and practical applications. Our study has exemplified this advance for the field of electronic memories and neuromorphic in-memory computing, and other atomistic ML models have been developed for a wide range of applications across different disciplines: recently published ML potentials have been used in the search for new stable inorganic crystals (e.g., for layered materials and solid-electrolyte candidates)<sup>86</sup>, in the prediction of supercritical behaviour in high-pressure liquid hydrogen, relevant to the structure and evolution of giant planets<sup>87</sup>, or in biomolecular-dynamics simulations of protein-folding processes and their thermodynamics<sup>88</sup>. The relevance of ML-driven simulations in the computational design of amorphous materials—PCMs and many others—has been pointed out in Ref. <sup>89</sup>. A very recent preprint discusses the role of ML potentials for device-scale modelling in a wider perspective<sup>90</sup>. We expect that our present work will stimulate the further development of efficient ML potentials for exploring structurally and chemically more complex PCM systems (e.g., incorporating interface effects of the surrounding materials in real-world devices), and provide a key approach for investigating scientific questions related to memory and computing applications.

## Methods

**The GST-ACE-24 potential.** All ACE models shown in the present work were fitted using `pacemaker` (Ref. <sup>40</sup>); their optimisation was carried out with XPOT (Ref. <sup>48</sup>). The extension of XPOT to ACE specifically, and the physical role of relevant hyperparameters, has been discussed in our more technical study in Ref. <sup>49</sup>. The latter includes investigations of ACE models for silicon and the binary compound  $\text{Sb}_2\text{Te}_3$  and provides a basis for the present work.

Using XPOT, we optimised 4 hyperparameters (cf. Supplementary Table 2) based on the iter-0 dataset and performed 32 fitting iterations (cf. Fig. 1b). To guide the target of the XPOT optimisation, we defined a testing dataset consisting of conventional disordered structures ( $\approx 200$  atoms each) and intermediate configurations during phase transitions (1,008 atoms each). These two types of structures were taken from AIMD simulations reported in Ref. <sup>31</sup> and Ref. <sup>18</sup>, respectively. This testing dataset was also used in the computation of RMSE values shown in Fig. 2c. In the XPOT optimisations, we first performed 8 exploratory fits using a Hammersley sequence to sample hyperparameters. Next, Bayesian Optimisation (BO) was used to optimise the hyperparameters over the remaining iterations. After XPOT optimisation, we “upfitted” the best potential (with an increased relative weighting of the energy; see Ref. <sup>49</sup>). In fact, after iter-3, we performed another XPOT run to determine whether the model required further hyperparameter optimisation based on the newly added configurations (i.e., those from iter-1 to iter-3). However, we found no notable improvements in accuracy on the testing dataset, and therefore continued with the existing hyperparameters as optimised on the iter-0 dataset. We note that the hyperparameters determined here for GST-ACE-24 were also used in fitting a separate ACE model for elemental tellurium, which is described in Ref. <sup>44</sup>.

The final potential model combines linear and nonlinear embeddings of the atomic neighbour environments over 3,000 basis functions and uses a radial cut-off of 8 Å. Training structures were weighted, based on their configuration types. Crystalline structures, melt–quench structures from AIMD, and RSS structures were given custom weightings to guide model accuracy in these regions. The model was fitted using an NVIDIA A100 GPU.

We note that a positive core-repulsion term can be included in ACE models to stop unphysical energies and forces from being produced at short atomic distances and to correct the core-repulsion behaviour, which can mitigate issues with “lost” atoms<sup>40</sup>; such an approach has been taken for the ACE models of Ref. <sup>38</sup>. By contrast, adding high-energy, small-scale random structures helps to explore a diverse configurational space (see, e.g., Refs. <sup>50,54</sup>). In particular, such additional configurations improve the ability of potentials to describe two-body

interactions at unusual distances, preventing the potentials from predicting the formation of clusters which, when evaluated with DFT, were found to be energetically unfavourable. We note that the addition of training data to represent short interatomic distances, “rather than relying on the core repulsion completely”, has been suggested by the `pacemaker` developers (see Ref. <sup>91</sup>). Our GST-ACE-24 model does not use a separate core-repulsion term.

**Validation.** We computed different structural properties of various amorphous GST compounds along the GeTe–Sb<sub>2</sub>Te<sub>3</sub> compositional tie-line, such as radial and angular distribution functions (Supplementary Fig. 4), and found that the predictions of our GST-ACE-24 model agreed very well with the AIMD data of Ref. <sup>31</sup>. Also, our ACE model faithfully reproduced the fraction of homopolar bonds, tetrahedral motifs, as well as the degree of local bond-length asymmetry (Supplementary Fig. 4), which are important structural factors that have been discussed in the context of ageing phenomena in the amorphous phase<sup>85</sup>. These structural validations demonstrate that our new ACE potential is both structurally and chemically transferable and can accurately describe disordered GST structures across various compositions, consistent with results for the GST-GAP-22 model<sup>31</sup>.

**Computational performance.** A key point in the present study is how ACE allows for ultra-fast device-scale simulations on a CPU-based high-performance computing system, without requiring GPU hardware at runtime. In addition to the simple and fast summation operations performed in the construction and inference of the ACE model, a recursive evaluation algorithm is used to construct the basis functions, reducing the number of arithmetic operations, and thus improving numerical efficiency<sup>39</sup>. We measured the performance of our GST-ACE-24 model by comparing against the published GST-GAP-22 potential<sup>31</sup> on the CPU cores of the ARCHER2 system. The compute nodes each have 128 CPU cores, and the memory per node is either 256 GB (standard nodes) or 512 GB (high-memory nodes); see Ref. <sup>92</sup> for details. The comparison between ACE and GAP is shown in Figs. 1c–e.

In addition, we compared the computational efficiency of GST-ACE-24 with a directly re-fitted equivariant neural-network potential, based on the MACE architecture<sup>34,55</sup>, on a GPU. This directly re-fitted MACE model used the same training dataset of GST-ACE-24. We performed the tests for GST-ACE-24 and the MACE model on an NVIDIA A100 GPU with 80 GB of memory, using a 10,000-atom structural model. The computational efficiency of GST-ACE-24 in this setting was  $\approx 2$  million MD steps per day, whereas the computational efficiency of the MACE model was  $\approx 335,000$  MD steps per day.

**DFT computations.** The AIMD data used for the fitting process (Fig. 1b) and the validation (Supplementary Fig. 4) of our ACE model were taken from our previous work (Ref. <sup>31</sup>). These AIMD simulations had been carried out using the “second-generation” Car–Parrinello scheme, as implemented in the Quickstep code of CP2K<sup>93</sup>, a combination of Gaussian-type and plane-wave basis sets, scalar-relativistic Goedecker pseudopotentials<sup>94</sup>, and the Perdew–Burke–Ernzerhof (PBE) functional<sup>47</sup>. Details of the AIMD simulations may be found in Ref. <sup>31</sup>.

To label the reference dataset, we computed the per-structure energies and per-atom forces by performing single-point DFT computations using the Vienna Ab initio Simulation Package (VASP)<sup>95,96</sup> with projector augmented-wave (PAW) pseudopotentials<sup>97,98</sup>. We used a 600 eV cut-off for plane waves and an energy tolerance of  $10^{-7}$  eV per cell for SCF convergence. An automatically generated  $k$ -point grid with a maximum spacing of  $0.2 \text{ \AA}^{-1}$  was used to sample reciprocal space.

**Molecular-dynamics simulations.** MD simulations were carried out with the GST-GAP-22 (Ref. <sup>31</sup>) and GST-ACE-24 ML potential models, using LAMMPS<sup>99</sup>, with interfaces to QUIP and `pacemaker`, respectively. The canonical ensemble (NVT) and the microcanonical ensemble (NVE) were used in this work. A Langevin thermostat was used to control the temperature in the NVT simulations. We simulated non-isothermal heating processes in the NVE ensemble. Additional energy was added to the kinetic energy of the atoms in the programming regions (Supplementary Note 3), with a timestep of 2 ps. The timestep for all ML-driven MD simulations was 2 fs. Structures were visualised using OVITO<sup>81</sup>.

## **Acknowledgements**

Y.Z. acknowledges a China Scholarship Council-University of Oxford scholarship. S.R.E. acknowledges the Leverhulme Trust (UK) for a Fellowship. W.Z. thanks support by the National Key Research and Development Program of China (2023YFB4404500), the National Natural Science Foundation of China (62374131), the Computing Centre in Xi'an and the International Joint Laboratory for Micro/Nano Manufacturing and Measurement Technologies of XJTU. V.L.D. acknowledges a UK Research and Innovation Frontier Research grant [grant number EP/X016188/1]. We are grateful for computational support from the UK national high-performance computing service, ARCHER2, for which access was obtained via the UKCP consortium and funded by EPSRC grant ref EP/X035891/1, as well as through a separate EPSRC Access to High-Performance Computing award.

## **Author contributions**

Y.Z., W.Z., and V.L.D. designed the study. Y.Z. and D.F.T.d.T. parameterised the ACE potential models. D.F.T.d.T. studied the role of hyperparameters and provided technical advice. Y.Z. carried out the large-scale molecular-dynamics simulations and visualised the results. All authors contributed to discussions and to the writing of the paper.

## **Data availability**

Data supporting the present study will be made openly available via Zenodo upon journal publication.

## References

1. Zhang, W., Mazzarello, R., Wuttig, M. & Ma, E. Designing crystallization in phase-change materials for universal memory and neuro-inspired computing. *Nat. Rev. Mater.* **4**, 150–168 (2019).
2. Feldmann, J., Youngblood, N., Wright, C. D., Bhaskaran, H. & Pernice, W. H. P. All-optical spiking neurosynaptic networks with self-learning capabilities. *Nature* **569**, 208–214 (2019).
3. Pellizzer, F., Pirovano, A., Bez, R. & Meyer, R. L. Status and perspectives of chalcogenide-based CrossPoint memories. In *2023 International Electron Devices Meeting (IEDM)* 1–4 (2023). DOI: 10.1109/IEDM45741.2023.10413669.
4. Ambrogio, S. *et al.* An analog-AI chip for energy-efficient speech recognition and transcription. *Nature* **620**, 768–775 (2023).
5. Le Gallo, M. *et al.* A 64-core mixed-signal in-memory compute chip based on phase-change memory for deep neural network inference. *Nat. Electron.* **6**, 680–693 (2023).
6. Zhou, W., Shen, X., Yang, X., Wang, J. & Zhang, W. Fabrication and integration of photonic devices for phase-change memory and neuromorphic computing. *Int. J. Extrem. Manuf.* **6**, 022001 (2024).
7. Wuttig, M. & Yamada, N. Phase-change materials for rewriteable data storage. *Nat. Mater.* **6**, 824–832 (2007).
8. Tuma, T., Pantazi, A., Le Gallo, M., Sebastian, A. & Eleftheriou, E. Stochastic phase-change neurons. *Nat. Nanotechnol.* **11**, 693–699 (2016).
9. Akola, J. & Jones, R. Structural phase transitions on the nanoscale: The crucial pattern in the phase-change materials  $\text{Ge}_2\text{Sb}_2\text{Te}_5$  and  $\text{GeTe}$ . *Phys. Rev. B* **76**, 235201 (2007).
10. Caravati, S., Bernasconi, M., Kühne, T. D., Krack, M. & Parrinello, M. Coexistence of tetrahedral- and octahedral-like sites in amorphous phase change materials. *Appl. Phys. Lett.* **91**, 171906 (2007).
11. Xu, M., Cheng, Y., Sheng, H. & Ma, E. Nature of atomic bonding and atomic structure in the phase-change  $\text{Ge}_2\text{Sb}_2\text{Te}_5$  Glass. *Phys. Rev. Lett.* **103**, 195502 (2009).
12. Huang, B. & Robertson, J. Bonding origin of optical contrast in phase-change memory materials. *Phys. Rev. B* **81**, 081204(R) (2010).
13. Raty, J.-Y. *et al.* A quantum-mechanical map for bonding and properties in solids. *Adv. Mater.* **31**, 1806280 (2019).
14. Wang, X.-D. *et al.* Multiscale simulations of growth-dominated  $\text{Sb}_2\text{Te}$  phase-change material for non-volatile photonic applications. *npj Comput. Mater.* **9**, 136 (2023).
15. Shen, X., Chu, R., Jiang, Y. & Zhang, W. Progress on materials design and multiscale simulations for phase-change memory. *Acta Metall. Sin.* **60**, 1362–1378 (2024).



16. Hegedüs, J. & Elliott, S. R. Microscopic origin of the fast crystallization ability of Ge-Sb-Te phase-change memory materials. *Nat. Mater.* **7**, 399–405 (2008).
17. Kalikka, J., Akola, J. & Jones, R. O. Crystallization processes in the phase change material Ge<sub>2</sub>Sb<sub>2</sub>Te<sub>5</sub>: Unbiased density functional/molecular dynamics simulations. *Phys. Rev. B* **94**, 134105 (2016).
18. Xu, Y. *et al.* Unraveling crystallization mechanisms and electronic structure of phase-change materials by large-scale ab initio simulations. *Adv. Mater.* **34**, 2109139 (2022).
19. Behler, J. First principles neural network potentials for reactive simulations of large molecular and condensed systems. *Angew. Chem. Int. Ed.* **56**, 12828–12840 (2017).
20. Deringer, V. L., Caro, M. A. & Csányi, G. Machine learning interatomic potentials as emerging tools for materials science. *Adv. Mater.* **31**, 1902765 (2019).
21. Friederich, P., Häse, F., Proppe, J. & Aspuru-Guzik, A. Machine-learned potentials for next-generation matter simulations. *Nat. Mater.* **20**, 750–761 (2021).
22. Sosso, G. C., Miceli, G., Caravati, S., Behler, J. & Bernasconi, M. Neural network interatomic potential for the phase change material GeTe. *Phys. Rev. B* **85**, 174103 (2012).
23. Behler, J. & Parrinello, M. Generalized neural-network representation of high-dimensional potential-energy surfaces. *Phys. Rev. Lett.* **98**, 146401 (2007).
24. Sosso, G. C., Salvalaglio, M., Behler, J., Bernasconi, M. & Parrinello, M. Heterogeneous crystallization of the phase change material GeTe via atomistic simulations. *J. Phys. Chem. C* **119**, 6428–6434 (2015).
25. Abou El Kheir, O., Bonati, L., Parrinello, M. & Bernasconi, M. Unraveling the crystallization kinetics of the Ge<sub>2</sub>Sb<sub>2</sub>Te<sub>5</sub> phase change compound with a machine-learned interatomic potential. *npj Comput. Mater.* **10**, 33 (2024).
26. Gabardi, S. *et al.* Atomistic simulations of the crystallization and aging of GeTe nanowires. *J. Phys. Chem. C* **121**, 23827–23838 (2017).
27. Mocanu, F. C. *et al.* Modeling the phase-change memory material, Ge<sub>2</sub>Sb<sub>2</sub>Te<sub>5</sub>, with a machine-learned interatomic potential. *J. Phys. Chem. B* **122**, 8998–9006 (2018).
28. Dragoni, D., Behler, J. & Bernasconi, M. Mechanism of amorphous phase stabilization in ultrathin films of monoatomic phase change material. *Nanoscale* **13**, 16146–16155 (2021).
29. Mo, P. *et al.* Accurate and efficient molecular dynamics based on machine learning and non von Neumann architecture. *npj Comput. Mater.* **8**, 107 (2022).
30. Bartók, A. P., Payne, M. C., Kondor, R. & Csányi, G. Gaussian approximation potentials: the accuracy of quantum mechanics, without the electrons. *Phys. Rev. Lett.* **104**, 136403 (2010).
31. Zhou, Y., Zhang, W., Ma, E. & Deringer, V. L. Device-scale atomistic modelling of phase-change memory materials. *Nat. Electron.* **6**, 746–754 (2023).

32. Li, K., Liu, B., Zhou, J. & Sun, Z. Revealing the crystallization dynamics of Sb–Te phase change materials by large-scale simulations. *J. Mater. Chem. C* **12**, 3897–3906 (2024).
33. Batzner, S. *et al.* E(3)-equivariant graph neural networks for data-efficient and accurate interatomic potentials. *Nat. Commun.* **13**, 2453 (2022).
34. Batatia, I., Kovács, D. P., Simm, G. N. C., Ortner, C. & Csányi, G. MACE: higher order equivariant message passing neural networks for fast and accurate force fields. Preprint at arXiv:2206.07697 (2023).
35. Wang, G., Sun, Y., Zhou, J. & Sun, Z. PotentialMind: graph convolutional machine learning potential for Sb–Te binary compounds of multiple stoichiometries. *J. Phys. Chem. C* **127**, 24724–24733 (2023).
36. Chang, C., Deringer, V. L., Katti, K. S., Van Speybroeck, V. & Wolverton, C. M. Simulations in the era of exascale computing. *Nat. Rev. Mater.* **8**, 309–313 (2023).
37. Drautz, R. Atomic cluster expansion for accurate and transferable interatomic potentials. *Phys. Rev. B* **99**, 014104 (2019).
38. Dunton, O. R., Arbaugh, T. & Starr, F. W. Computationally efficient machine-learned model for GST phase change materials via direct and indirect learning. *J. Chem. Phys.* **162**, 034501 (2025).
39. Lysogorskiy, Y. *et al.* Performant implementation of the atomic cluster expansion (PACE) and application to copper and silicon. *npj Comput. Mater.* **7**, 97 (2021).
40. Bochkarev, A. *et al.* Efficient parametrization of the atomic cluster expansion. *Phys. Rev. Mater.* **6**, 013804 (2022).
41. Dusson, G. *et al.* Atomic cluster expansion: Completeness, efficiency and stability. *J. Comput. Phys.* **454**, 110946 (2022).
42. Deringer, V. L. *et al.* Gaussian process regression for materials and molecules. *Chem. Rev.* **121**, 10073–10141 (2021).
43. Qamar, M., Mrovec, M., Lysogorskiy, Y., Bochkarev, A. & Drautz, R. Atomic cluster expansion for quantum-accurate large-scale simulations of carbon. *J. Chem. Theory Comput.* **19**, 5151–5167 (2023).
44. Zhou, Y., Elliott, S. R., Toit, D. F. T. du, Zhang, W. & Deringer, V. L. The pathway to chirality in elemental tellurium. Preprint at arXiv:2409.03860 (2024).
45. Erhard, L. C., Rohrer, J., Albe, K. & Deringer, V. L. Modelling atomic and nanoscale structure in the silicon–oxygen system through active machine learning. *Nat. Commun.* **15**, 1927 (2024).
46. Morrow, J. D. & Deringer, V. L. Indirect learning and physically guided validation of interatomic potential models. *J. Chem. Phys.* **157**, 104105 (2022).
47. Perdew, J. P., Burke, K. & Ernzerhof, M. Generalized gradient approximation made simple. *Phys. Rev. Lett.* **77**, 3865–3868 (1996).

48. Thomas du Toit, D. F. & Deringer, V. L. Cross-platform hyperparameter optimization for machine learning interatomic potentials. *J. Chem. Phys.* **159**, 024803 (2023).
49. Thomas du Toit, D. F., Zhou, Y. & Deringer, V. L. Hyperparameter optimization for atomic cluster expansion potentials. *J. Chem. Theory Comput.* **20**, 10103–10113 (2024).
50. Pickard, C. J. & Needs, R. J. High-pressure phases of silane. *Phys. Rev. Lett.* **97**, 045504 (2006).
51. Pickard, C. J. & Needs, R. J. Ab initio random structure searching. *J. Phys.: Condens. Matter* **23**, 053201 (2011).
52. Deringer, V. L., Proserpio, D. M., Csányi, G. & Pickard, C. J. Data-driven learning and prediction of inorganic crystal structures. *Faraday Discuss.* **211**, 45–59 (2018).
53. Deringer, V. L., Pickard, C. J. & Csányi, G. Data-driven learning of total and local energies in elemental boron. *Phys. Rev. Lett.* **120**, 156001 (2018).
54. Bernstein, N., Csányi, G. & Deringer, V. L. De novo exploration and self-guided learning of potential-energy surfaces. *npj Comput. Mater.* **5**, 99 (2019).
55. Batatia, I. *et al.* The design space of E(3)-equivariant atom-centred interatomic potentials. *Nat. Mach. Intell.* **7**, 56–67 (2025).
56. Stocker, S., Gasteiger, J., Becker, F., Günnemann, S. & Margraf, J. T. How robust are modern graph neural network potentials in long and hot molecular dynamics simulations? *Mach. Learn.: Sci. Technol.* **3**, 045010 (2022).
57. Unke, O. T. *et al.* Machine learning force fields. *Chem. Rev.* **121**, 10142–10186 (2021).
58. Ben Mahmoud, C., Gardner, J. L. A. & Deringer, V. L. Data as the next challenge in atomistic machine learning. *Nat. Comput. Sci.* **4**, 384–387 (2024).
59. Allen, A. E. A. *et al.* Learning together: Towards foundation models for machine learning interatomic potentials with meta-learning. *npj Comput. Mater.* **10**, 154 (2024).
60. Liu, Y. *et al.* An automated framework for exploring and learning potential-energy surfaces. Preprint at arXiv:2412.16736 (2024).
61. Deringer, V. L., Caro, M. A. & Csányi, G. A general-purpose machine-learning force field for bulk and nanostructured phosphorus. *Nat. Commun.* **11**, 5461 (2020).
62. Pickard, C. J. Ephemeral data derived potentials for random structure search. *Phys. Rev. B* **106**, 014102 (2022).
63. Pickard, C. J. Beyond theory-driven discovery: introducing hot random search and datum-derived structures. *Faraday Discuss.* **256**, 61–84 (2025).
64. Bartók, A. P., Kondor, R. & Csányi, G. On representing chemical environments. *Phys. Rev. B* **87**, 184115 (2013).

65. Welnic, W. & Wuttig, M. Reversible switching in phase-change materials. *Mater. Today* **11**, 20–27 (2008).
66. Loke, D. *et al.* Breaking the speed limits of phase-change memory. *Science* **336**, 1566–1569 (2012).
67. Loke, D. K. *et al.* Ultrafast nanoscale phase-change memory enabled by single-pulse conditioning. *ACS Appl. Mater. Interfaces* **10**, 41855–41860 (2018).
68. Li, Z., Si, C., Zhou, J., Xu, H. & Sun, Z. Yttrium-doped Sb<sub>2</sub>Te<sub>3</sub>: a promising material for phase-change memory. *ACS Appl. Mater. Interfaces* **8**, 26126–26134 (2016).
69. Rao, F. *et al.* Reducing the stochasticity of crystal nucleation to enable subnanosecond memory writing. *Science* **358**, 1423–1427 (2017).
70. Wang, Y. *et al.* Scandium doped Ge<sub>2</sub>Sb<sub>2</sub>Te<sub>5</sub> for high-speed and low-power-consumption phase change memory. *Appl. Phys. Lett.* **112**, 133104 (2018).
71. Hu, S., Xiao, J., Zhou, J., Elliott, S. R. & Sun, Z. Synergy effect of co-doping Sc and Y in Sb<sub>2</sub>Te<sub>3</sub> for phase-change memory. *J. Mater. Chem. C* **8**, 6672–6679 (2020).
72. Wang, X.-P. *et al.* Time-dependent density-functional theory molecular-dynamics study on amorphization of Sc-Sb-Te alloy under optical excitation. *npj Comput. Mater.* **6**, 31 (2020).
73. Ronneberger, I., Zhang, W., Eshet, H. & Mazzarello, R. Crystallization properties of the Ge<sub>2</sub>Sb<sub>2</sub>Te<sub>5</sub> phase-change compound from advanced simulations. *Adv. Funct. Mater.* **25**, 6407–6413 (2015).
74. Laio, A. & Parrinello, M. Escaping free-energy minima. *Proc. Natl. Acad. Sci. U. S. A.* **99**, 12562–12566 (2002).
75. Kalikka, J., Akola, J., Larrucea, J. & Jones, R. O. Nucleus-driven crystallization of amorphous Ge<sub>2</sub>Sb<sub>2</sub>Te<sub>5</sub>: A density functional study. *Phys. Rev. B* **86**, 144113 (2012).
76. Zhang, B. *et al.* Vacancy structures and melting behavior in rock-salt GeSbTe. *Sci. Rep.* **6**, 25453 (2016).
77. Energy use and emissions. <https://docs.archer2.ac.uk/user-guide/energy/>.
78. Song, Z. *et al.* 12-state multi-level cell storage implemented in a 128 Mb phase change memory chip. *Nanoscale* **13**, 10455–10461 (2021).
79. Abou El Kheir, O. & Bernasconi, M. Million-atom simulation of the set process in phase change memories at the real device scale. Preprint at arXiv:2501.07384 (2025).
80. Larsen, P. M., Schmidt, S. & Schiøtz, J. Robust structural identification via polyhedral template matching. *Model. Simul. Mater. Sci. Eng.* **24**, 055007 (2016).
81. Stukowski, A. Visualization and analysis of atomistic simulation data with OVITO—the Open Visualization Tool. *Model. Simul. Mater. Sci. Eng.* **18**, 015012 (2010).

82. Nandakumar, S. R. *et al.* A phase-change memory model for neuromorphic computing. *J. Appl. Phys.* **124**, 152135 (2018).
83. Sebastian, A. *et al.* Tutorial: Brain-inspired computing using phase-change memory devices. *J. Appl. Phys.* **124**, 111101 (2018).
84. Zhang, W. & Ma, E. Unveiling the structural origin to control resistance drift in phase-change memory materials. *Mater. Today* **41**, 156–176 (2020).
85. Raty, J. Y. *et al.* Aging mechanisms in amorphous phase-change materials. *Nat. Commun.* **6**, 7467 (2015).
86. Merchant, A. *et al.* Scaling deep learning for materials discovery. *Nature* **624**, 80–85 (2023).
87. Cheng, B., Mazzola, G., Pickard, C. J. & Ceriotti, M. Evidence for supercritical behaviour of high-pressure liquid hydrogen. *Nature* **585**, 217–220 (2020).
88. Wang, T. *et al.* Ab initio characterization of protein molecular dynamics with AI<sup>2</sup>BMD. *Nature* **635**, 1019–1027 (2024).
89. Liu, Y., Madanchi, A., Anker, A. S., Simine, L. & Deringer, V. L. The amorphous state as a frontier in computational materials design. *Nat. Rev. Mater.*, DOI: 10.1038/s41578-024-00754-2 (2024).
90. Miret, S., Lee, K. L. K., Gonzales, C., Mannan, S. & Krishnan, N. M. A. Energy & force regression on DFT trajectories is not enough for universal machine learning interatomic potentials. Preprint at arXiv:2502.03660 (2025).
91. Frequently asked questions (FAQ).  
<https://pacemaker.readthedocs.io/en/latest/pacemaker/faq>.
92. Beckett, G. *et al.* *ARCHER2 Service Description*. <https://zenodo.org/records/14507040>, DOI: 10.5281/zenodo.14507040 (2024).
93. Kühne, T. D. *et al.* CP2K: An electronic structure and molecular dynamics software package - Quickstep: Efficient and accurate electronic structure calculations. *J. Chem. Phys.* **152**, 194103 (2020).
94. Goedecker, S., Teter, M. & Hutter, J. Separable dual-space Gaussian pseudopotentials. *Phys. Rev. B* **54**, 1703 (1996).
95. Kresse, G. & Hafner, J. Ab initio molecular dynamics for liquid metals. *Phys. Rev. B* **47**, 558–561 (1993).
96. Kresse, G. & Furthmüller, J. Efficient iterative schemes for ab initio total-energy calculations using a plane-wave basis set. *Phys. Rev. B* **54**, 11169–11186 (1996).
97. Blöchl, P. E. Projector augmented-wave method. *Phys. Rev. B* **50**, 17953–17979 (1994).
98. Kresse, G. & Joubert, D. From ultrasoft pseudopotentials to the projector augmented-wave method. *Phys. Rev. B* **59**, 1758 (1999).

99. Thompson, A. P. *et al.* LAMMPS - a flexible simulation tool for particle-based materials modeling at the atomic, meso, and continuum scales. *Comput. Phys. Commun.* **271**, 108171 (2022).

Supplementary Information for

## **Full-cycle device-scale simulations of memory materials with a tailored atomic-cluster-expansion potential**

Yuxing Zhou,<sup>1</sup> Daniel F. Thomas du Toit,<sup>1</sup> Stephen R. Elliott,<sup>2</sup> Wei Zhang,<sup>3,\*</sup> and Volker L. Deringer<sup>1,\*</sup>

<sup>1</sup>*Inorganic Chemistry Laboratory, Department of Chemistry, University of Oxford, Oxford OX1 3QR, United Kingdom*

<sup>2</sup>*Physical and Theoretical Chemistry Laboratory, Department of Chemistry, University of Oxford, Oxford OX1 3QZ, United Kingdom*

<sup>3</sup>*Center for Alloy Innovation and Design (CAID), State Key Laboratory for Mechanical Behavior of Materials, Xi'an Jiaotong University, Xi'an 710049, China*

\*E-mail: wzhang0@mail.xjtu.edu.cn; volker.deringer@chem.ox.ac.uk

This document contains:

### **Supplementary Note 1**

*Components of the reference dataset* S2

### **Supplementary Note 2**

*Validation and computational efficiency tests* S3

### **Supplementary Note 3**

*Simulation protocols for device-scale modelling* S4

Supplementary Tables S5–S6

Supplementary Figures S7–S10

Supplementary References S11

## Supplementary Note 1 (Components of the reference dataset)

We here provide more details about the construction of the reference dataset for the ACE potential model fitted in the present work (referred to as “GST-ACE-24” in the following). An overview of the fitting protocol for GST-ACE-24 is shown in Fig. 1b of the main text. We started from the training dataset of our previously published GAP potential<sup>S1</sup> (referred to as “GST-GAP-22” in the following). We first re-labelled the GST-GAP-22 dataset using DFT with the Perdew–Burke–Ernzerhof (PBE) exchange–correlation functional<sup>S2</sup>. We added 59 amorphous and supercooled liquid structures of different GST compositions into the iter-0 dataset: these AIMD configurations were taken from melt-quench AIMD simulations using PBE, reported in Ref. <sup>S1</sup>, and re-labelled here using single-point DFT computations. We then carried out the first XPOT-based hyperparameter optimisation.

Next, five iterations were carried out to gradually expand the training dataset for the ACE potential. From iter-1 to iter-3, we added domain-relevant configurations, including the melt-quenched structures and the intermediate configurations during the crystallisation and melting processes. In these iterations, the previous version of the ACE model was used to run independent ACE-driven MD (ACE-MD) simulations, in which new structural models were collected randomly from the ACE-MD trajectories. To obtain the domain-specific configurations for crystallisation, we started from crystal structures of GST. Some atomic layers were manually fixed during the melt-quench simulations. We then annealed these partially crystalline structures at elevated temperatures (e.g., 500–700 K). Due to the existence of pre-fixed crystalline layers (or seeds), the structural models started to recrystallise. We then randomly took intermediate configurations during the recrystallisation processes and added them into the training dataset. To collect the domain-specific configurations for melting, we started from crystal structures of GST. We then heated the crystal structures from 300 K to above their melting points. During the heating process, we collected the configurations in which some local structural disordering started to appear, which represented the starting of melting.

In addition, to increase the robustness of the ACE model, we added some small-scale (6–40 atoms) hard-sphere random structures of different chemical compositions in iter-1 to iter-3, generated using the `buildcell` code of the *ab initio* random structure searching (AIRSS) code<sup>S3,S4</sup>. As shown in the ablation studies presented in the main text (cf. Fig. 2), including some random structures with short atomic distances can help prevent failures caused by lost atoms in ACE-MD simulations. After iter-3, we performed a second XPOT run (which, however, did not notably improve the model, and therefore we continued with the previous hyperparameters).

To further improve the robustness of our ACE models in ACE-MD simulations, we also carried out ACE-driven random structure searching (ACE-RSS, akin to AIRSS<sup>S3,S4</sup> and GAP-RSS<sup>S5,S6</sup>) in two other iterations (iter-4 and iter-5). We note that ACE-RSS could not be carried out in iter-1 to iter-3, because some relaxations failed due to lost atoms. However, as more randomly generated structures were accumulated, successful ACE-RSS runs further explored the potential-energy surface by incorporating the relaxation of such random structures.

The resultant training dataset included 1,944 new training structures. All structures were labelled with the PBE functional. A summary of the composition of the training dataset for GST-ACE-24 is given in Supplementary Table 1.



## Supplementary Note 2 (Validation and computational efficiency tests)

We carried out comprehensive validation studies of our ACE models, including numerical and physically-guided validation, following ideas discussed in Ref. <sup>S7</sup>. We performed comprehensive ablation studies, as shown in Fig. 2 of the main text. In these ablation studies, we gradually removed the training structures from the GST-ACE-24 dataset, or we changed the hyperparameters used in the ACE models. We constructed a testing dataset which consists of conventional disordered GST structures (containing  $\approx 200$  atoms) and intermediate configurations during the phase-transition processes (containing 1,008 atoms). The former were taken from melt-quench AIMD simulations as reported in Ref. <sup>S1</sup>, and the latter were taken from AIMD crystallisation simulations as shown in Ref. <sup>S8</sup>. This testing dataset was labelled using DFT with PBE, and we then computed the root mean square error (RMSE) of energy and forces for different ACE models, based on the testing dataset.

To test the computational efficiency of GST-ACE-24 as compared to the previously reported GST-GAP-22 model, we carried out ACE- and GAP-driven MD simulations on the CPU nodes of ARCHER2, a high-performance computing system in the UK. The compute nodes each have 128 cores, which are dual-socket nodes with two 64-core AMD EPYC 7742 processors (see details at Ref. <sup>S9</sup>). The same MD protocol was used to evaluate the computational efficiency: the structural models were annealed at 1,000 K for 2 ps (i.e., 1,000 MD steps). The total running time was measured to indicate the computational speed. The memory per node is 256 GB (standard nodes) or 512 GB (high-memory nodes). A large efficiency gap was observed between ACE-MD and GAP-MD—ACE-MD is more than  $400 \times$  times faster than GAP-MD. More importantly, GAP-MD simulations require larger memory sizes, and simulations of more than 1 million atoms failed due to the lack of memory. In contrast, ACE-MD is more memory-efficient and can be used in device-scale simulations up to one billion atoms (cf. Fig. 1 in the main text and Supplementary Fig. 1).

### Supplementary Note 3 (Simulation protocols for device-scale modelling)

We here discuss the construction of structural models of different device setups<sup>S1</sup> and the simulation protocols for the device-scale modelling performed in Ref. <sup>S1</sup> and in the present work.

We first discuss how to construct the structural models of Ge<sub>1</sub>Sb<sub>2</sub>Te<sub>4</sub> for two different device architectures, *viz.* the cross-point and mushroom-type devices. For the cross-point device, we used a simulation box of 20 × 20 × 40 nm<sup>3</sup> which contains 532,980 atoms, as in Ref. <sup>S1</sup>. We first constructed an amorphous slab of Ge<sub>1</sub>Sb<sub>2</sub>Te<sub>4</sub> (20 × 20 × 0.8 nm<sup>3</sup>) via a melt-quench simulation. This slab was placed on the top of the cell and was fixed during all ACE-MD simulations, serving as a heat barrier to stop unwanted atomic migrations across the periodic box. To construct a structural model for mushroom-type devices, we built a 100 × 40 × 5 nm<sup>3</sup> slab model (containing 794,808 atoms), which represents the cross-section of 100 × 40 nm<sup>2</sup> in the middle of a mushroom-type cell (cf. Fig. 4b in the main text). We also fixed a 6-nm thick slab of amorphous Ge<sub>1</sub>Sb<sub>2</sub>Te<sub>4</sub> on the top of this cross-section model as a heat barrier. We note that these heat barriers shown in both structural models reflect the thermal barriers that are in contact with the GST material in real-world GST devices.

Next, we describe how to simulate the non-isothermal heating and cooling processes caused by the RESET pulses. To simulate the non-isothermal heating process, which is triggered by a short and intense external heating pulse, we used the NVE ensemble. We gradually added kinetic energy to the atoms in the programming regions. These added kinetic-energy values were spatially inhomogeneous, in a linear way along the *z*-axis. More energy was added to the atoms close to the bottom whereas less energy was added to the atoms on the top. By doing this, a temperature gradient from the bottom to the top of the cell was created (Supplementary Figures 2 and 3), reflecting a non-isothermal heating process.

To model the heat-dissipation process after the heating pulse, we gradually removed the kinetic energy from the atoms in the programming region. The amount of energy removed from a given atom depends on its atomic temperature. We note that the “atomic temperature” discussed here is not a direct physical observable, but a concept used in MD simulations to describe the kinetic energy associated with the motion of an individual atom. In other words, the atomic temperature is instantaneous and is defined directly, based on its instantaneous kinetic energy (and velocity),

$$T_{\text{atom}} = \frac{2}{3k_{\text{B}}} \cdot E_{\text{kin}} = \frac{2}{3k_{\text{B}}} \cdot \frac{1}{2}mv^2,$$

in which  $T_{\text{atom}}$  is the instantaneous atomic temperature,  $E_{\text{kin}}$  is the instantaneous kinetic energy,  $k_{\text{B}}$  is the Boltzmann constant,  $m$  is the atomic mass, and  $v$  is the instantaneous velocity obtained from MD simulations. The instantaneous atomic temperature of a given atom will be compared to ambient temperature (*i.e.*, 300 K). The higher the instantaneous atomic temperature, the greater the amount of kinetic energy that will be removed. By doing this, we simulated the heat-dissipation process which also showed prominent temperature gradients (Supplementary Figures 2 and 3).

In contrast, the SET (crystallisation) processes in the present work were all modelled using the NVT ensemble. A Langevin thermostat, with a damping timescale of 0.04 ps (corresponding to a damping coefficient of 25 ps<sup>-1</sup>), was used to control the temperature.

## Supplementary Tables

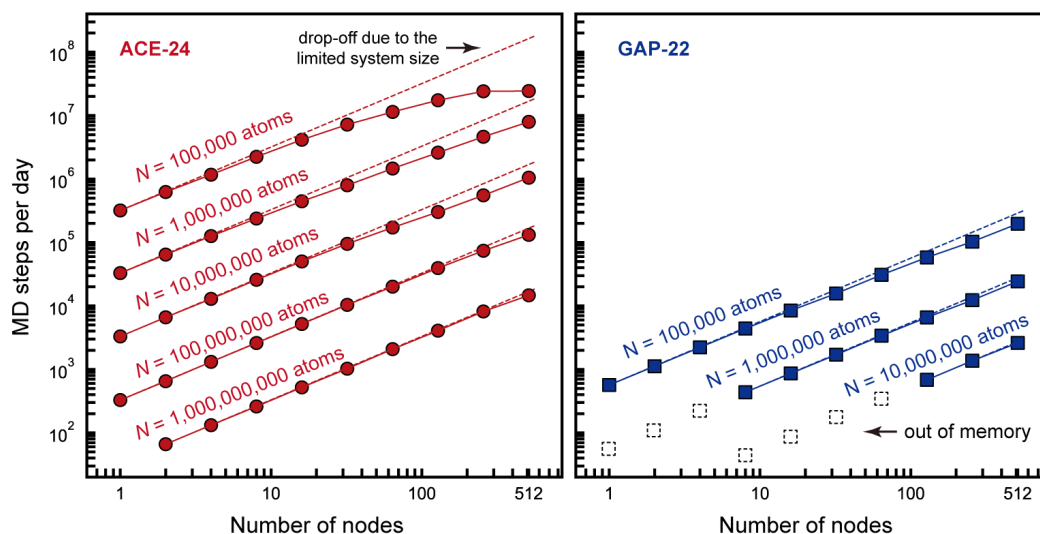
**Supplementary Table 1.** Summary of the composition of the GST-ACE-24 reference dataset.

Components	Descriptions	database size	
		Cells	Atoms
GST-GAP-22 (published in Ref. <sup>S1</sup> )	Free atom	3	3
	Dimer	210	420
	Crystalline structures	1261	69055
	AIMD structures (PBEsol level)	210	41490
	Melt-quenched disordered structures	336	65962
	Phase-transition configurations	672	164202
iter-0	AIMD structures (PBE level)	59	11484
	Melt-quenched disordered structures	196	30208
iter-1	Phase-transition configurations	168	43752
	Hard-sphere random structures	120	2317
	Melt-quenched disordered structures	140	25560
iter-2	Phase-transition configurations	167	43493
	Hard-sphere random structures	55	1390
	Melt-quenched disordered structures	140	25560
iter-3	Phase-transition configurations	168	43752
	Hard-sphere random structures	144	2090
iter-4	ACE-RSS structures	287	4602
iter-5	ACE-RSS structures	300	4132
<b>Total</b>		<b>4636</b>	<b>579472</b>

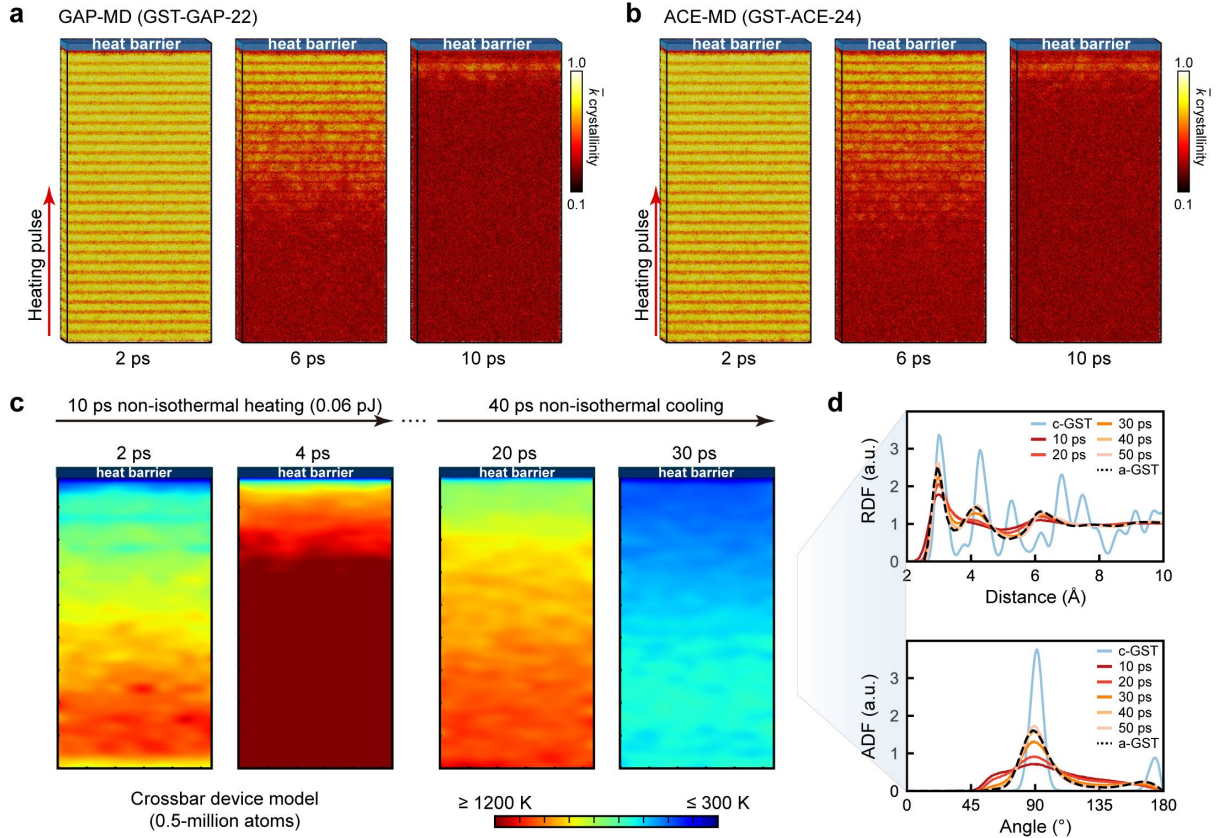
**Supplementary Table 2.** Optimised hyperparameters in the XPOT runs.

<b>Optimised hyperparameters</b>	<b>Descriptions</b>	<b>Hyperparameter ranges</b>	<b>Values after optimisation</b>
Cut-off	Cut-off distance (Å)	5.5 – 8.0	8.0
Radial parameter	Used in the construction of radial basis	4 – 10	10
Prefactor $k_2$	Used to define the embedding functions:	0.1 – 5	4.577
Prefactor $k_3$	$E_i = \varphi + k_2\sqrt{\varphi} + k_3\varphi^2$	0.1 – 5	0.101

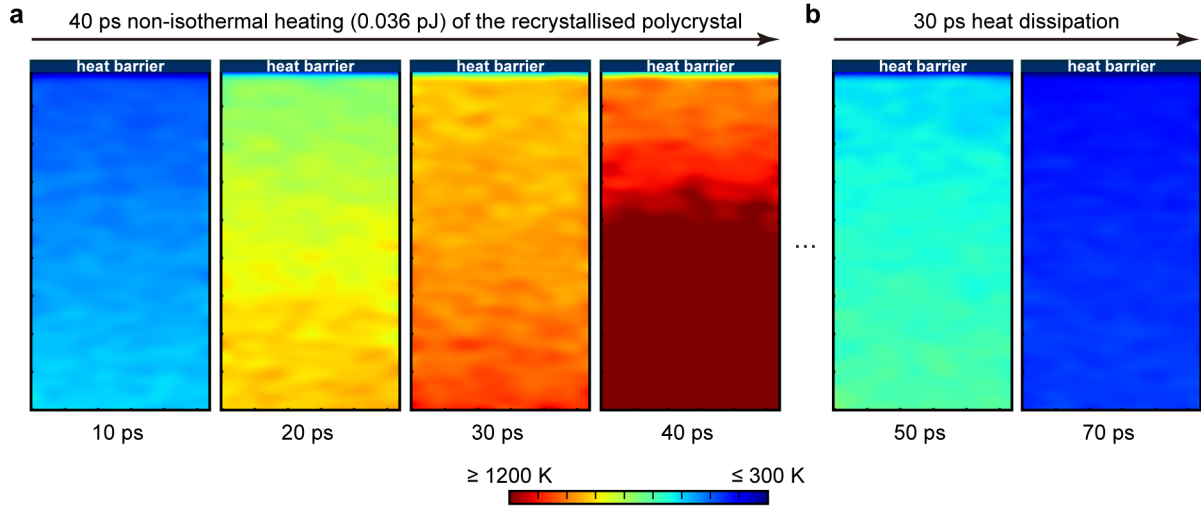
## Supplementary Figures



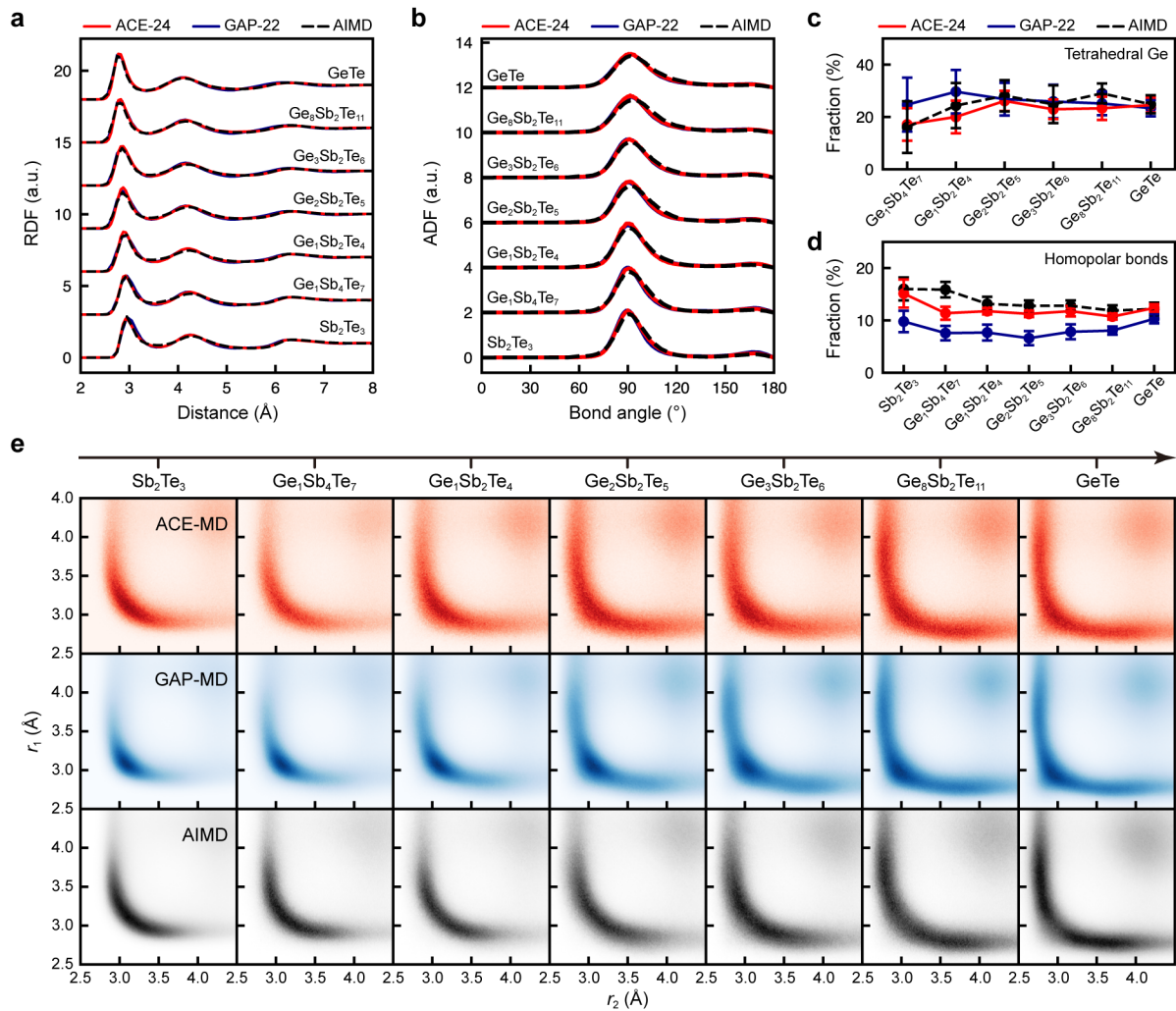
**Supplementary Fig. 1: Strong scaling tests for GST-ACE-24 and GST-GAP-22.** To evaluate the computational speed, a 2-ps (i.e., 1,000 MD steps) MD simulation was carried out. The numbers of MD steps achieved per day were then calculated and are plotted against the number of nodes. Different system sizes were tested, ranging from 100,000 atoms to 1,000,000,000 (1 billion) atoms; the results of GST-ACE-24 and GST-GAP-22 are indicated by filled circles and squares, respectively. The solid lines between points are guides to the eye; the dashed lines indicate ideal strong scaling behaviour. Note that some data points could not be measured when using GST-GAP-22 in the simulation of 1,000,000 atoms or more (“missing” filled squares in the right-hand panel), because GAP-MD failed due to a lack of memory: in these cases, we show empty dashed squares extrapolated from the ideal scaling lines.



**Supplementary Fig. 2: The non-isothermal RESET process of GST-based cross-point devices.** (a) Snapshots of a device-scale GAP-MD simulation (532,000 atoms) for  $\text{Ge}_1\text{Sb}_2\text{Te}_4$ , which was performed in this work using the GST-GAP-22 potential<sup>S1</sup>. The initial configuration is the (single-crystal) trigonal phase of  $\text{Ge}_1\text{Sb}_2\text{Te}_4$ . An  $\approx 8$  Å thick slab of amorphous GST was fixed on the top of the cell (near  $z = 40$  nm), serving as a heat barrier to stop atoms from migrating across the boundary of the periodic box. This setup differs from the initial structural model in Ref. <sup>S1</sup>, where a crystalline GST slab was used as the heat barrier. A 10-ps heating pulse (0.064 pJ) was added from the bottom to the top of cell to melt the structural model. (b) The same type of heating simulation as shown in panel (a), but now carried out using our new GST-ACE-24 potential. Colour coding in panels (a) and (b) indicates the SOAP-based per-atom crystallinity<sup>S8</sup>,  $\bar{k}$ , suggesting a gradual melting process from crystalline-like (*yellow*) to amorphous-like (*red*). (c) A simulation of the 40-ps heat-dissipation process was carried out using ACE-MD after the 10-ps heating pulse. The corresponding two-dimensional temperature profiles were calculated from the ACE-MD simulations for the non-isothermal RESET process, based on the approach described in Ref. <sup>S1</sup>. (d) The evolution of the GST structure from this heating-and-cooling process, characterised using both RDF and ADF results from the central area of the device-scale model (20 nm thick). We note that the structural features of amorphous  $\text{Ge}_1\text{Sb}_2\text{Te}_4$  obtained from the device-scale structural model agree well with those of small-scale bulk amorphous structures, modelled by AIMD in our previous work (Ref. <sup>S1</sup>). This figure is drawn in a style similar to Ref. <sup>S1</sup>.



**Supplementary Fig. 3: Temperature profiles of the RESET process for the recrystallised polycrystalline structure.** The RESET process included (a) a 40-ps heating (0.036 pJ) process and (b) a 30-ps heat dissipation process. The initial configuration of this RESET simulation was taken from the recrystallised polycrystalline structure of  $\text{Ge}_1\text{Sb}_2\text{Te}_4$  (cf. Fig. 3c in the main text). The atomic trajectory of this RESET process is shown in Fig. 3c of the main text. The technical details regarding the computation of the temperature profiles have been given in our previous work (Ref. <sup>S1</sup>).



**Supplementary Fig. 4: Local structure of amorphous GST compositions from ML-driven MD and AIMD simulations.** (a) Radial distribution functions (RDFs) for seven different compositions along the  $\text{GeTe}$ – $\text{Sb}_2\text{Te}_3$  tie-line. (b) Angular distribution function (ADF) for the seven compounds. (c) The calculated fraction of tetrahedral Ge atoms, defined by a bond-order parameter, as discussed in previous work<sup>S10</sup>. (d) Fraction of homopolar and “wrong” bonds, i.e., bonds between two cation-like atoms or two anion-like atoms (*viz.*  $\text{Ge}$ – $\text{Ge}$ ,  $\text{Ge}$ – $\text{Sb}$ ,  $\text{Sb}$ – $\text{Sb}$ , and  $\text{Te}$ – $\text{Te}$ ). (e) Angular-limited three-body correlation (ALTBC) functions for the amorphous structures of seven GST alloys. The ALTBC function expresses the probability of having a bond of length  $r_1$  almost aligned with another bond of length  $r_2$  with angular deviations smaller than  $30^\circ$ , providing a measure for the degrees of local distortion in the amorphous structures<sup>S11</sup>. Results for AIMD, GAP-MD, and ACE-MD structures are shown in black, blue, and red, respectively. All data shown in this figure present mean values over 6,000 snapshots of AIMD, GAP-MD, and ACE-MD simulations (which were collected from the last 40 ps trajectories of 3 independent melt-quench runs). The error bars in panel (c–d) indicate standard deviations over these 6,000 snapshots. This figure is drawn in a style similar to Ref. <sup>S1</sup>, and all structural analyses were performed using the same type of benchmarks as in that prior work: all AIMD and GAP-MD results were produced based on the atomic trajectories as reported in Ref. <sup>S1</sup>, and the AIMD and GAP-MD data in plotted panels (a) and (c) are taken from Ref. <sup>S1</sup>. Lines between points in panels (c–d) are guides to the eye.



## Supplementary References

- S1. Zhou, Y., Zhang, W., Ma, E. & Deringer, V. L. Device-scale atomistic modelling of phase-change memory materials. *Nat. Electron.* **6**, 746–754 (2023).
- S2. Perdew, J. P., Burke, K. & Ernzerhof, M. Generalized gradient approximation made simple. *Phys. Rev. Lett.* **77**, 3865–3868 (1996).
- S3. Pickard, C. J. & Needs, R. J. High-pressure phases of silane. *Phys. Rev. Lett.* **97**, 045504 (2006).
- S4. Pickard, C. J. & Needs, R. J. Ab initio random structure searching. *J. Phys.: Condens. Matter* **23**, 053201 (2011).
- S5. Deringer, V. L., Pickard, C. J. & Csányi, G. Data-driven learning of total and local energies in elemental boron. *Phys. Rev. Lett.* **120**, 156001 (2018).
- S6. Bernstein, N., Csányi, G. & Deringer, V. L. De novo exploration and self-guided learning of potential-energy surfaces. *npj Comput. Mater.* **5**, 99 (2019).
- S7. Morrow, J. D., Gardner, J. L. A. & Deringer, V. L. How to validate machine-learned interatomic potentials. *J. Chem. Phys.* **158**, 121501 (2023).
- S8. Xu, Y. *et al.* Unraveling crystallization mechanisms and electronic structure of phase-change materials by large-scale ab initio simulations. *Adv. Mater.* **34**, 2109139 (2022).
- S9. Beckett, G. *et al.* ARCHER2 Service Description. <https://zenodo.org/records/14507040>, DOI: 10.5281/zenodo.14507040 (2024).
- S10. Caravati, S., Bernasconi, M., Kühne, T. D., Krack, M. & Parrinello, M. Coexistence of tetrahedral- and octahedral-like sites in amorphous phase change materials. *Appl. Phys. Lett.* **91**, 171906 (2007).
- S11. Raty, J. Y. *et al.* Aging mechanisms in amorphous phase-change materials. *Nat. Commun.* **6**, 7467 (2015).